

Frontal Circulation and Submesoscale Variability during the Formation of a Southern Ocean Mesoscale Eddy

KATHERINE A. ADAMS,^a PHILIP HOSEGOOD,^a JOHN R. TAYLOR,^b JEAN-BAPTISTE SALLÉE,^c SCOTT BACHMAN,^b RICARDO TORRES,^d AND MEGAN STAMPER^b

^a School of Biological and Marine Sciences, Plymouth University, Plymouth, United Kingdom

^b Department of Applied Mathematics and Theoretical Physics, University of Cambridge, Cambridge, United Kingdom

^c Sorbonne Universités, UPMC/CNRS, LOCEAN Laboratory, Paris, France

^d Plymouth Marine Laboratory, Plymouth, United Kingdom

(Manuscript received 6 December 2016, in final form 19 April 2017)

ABSTRACT

Observations made in the Scotia Sea during the May 2015 Surface Mixed Layer Evolution at Submesoscales (SMILES) research cruise captured submesoscale, $O(1\text{--}10)$ km, variability along the periphery of a mesoscale $O(10\text{--}100)$ km meander precisely as it separated from the Antarctic Circumpolar Current (ACC) and formed a cyclonic eddy ~ 120 km in diameter. The meander developed in the Scotia Sea, an eddy-rich region east of the Drake Passage where the Subantarctic and Polar Fronts converge and modifications of Subantarctic Mode Water (SAMW) occur. In situ measurements reveal a rich submesoscale structure of temperature and salinity and a loss of frontal integrity along the newly formed southern sector of the eddy. A mathematical framework is developed to estimate vertical velocity from collocated drifter and horizontal water velocity time series, under certain simplifying assumptions appropriate for the current dataset. Upwelling (downwelling) rates of $O(100)$ m day $^{-1}$ are found in the northern (southern) eddy sector. Favorable conditions for submesoscale instabilities are found in the mixed layer, particularly at the beginning of the survey in the vicinity of density fronts. Shallower mixed layer depths and increased stratification are observed later in the survey on the inner edge of the front. Evolution in temperature–salinity ($T\text{--}S$) space indicates modification of water mass properties in the upper 200 m over 2 days. Modifications along $\sigma_\theta = 27\text{--}27.2$ kg m $^{-3}$ have climate-related implications for mode and intermediate water transformation in the Scotia Sea on finer spatiotemporal scales than observed previously.

1. Introduction

The Southern Ocean hosts the most energetic current system in the world, the Antarctic Circumpolar Current (ACC). Zonally unbounded by land, the ACC connects ocean basins and transports an estimated 173 Sv (1 Sv $\equiv 10^6 \text{ m}^3 \text{ s}^{-1}$) through the Drake Passage (Donohue et al. 2016). The ACC is predominantly in geostrophic balance with sea surface height (SSH) gradients and lateral density gradients, hereafter fronts. Large-scale instabilities in the balanced ACC flow cause mesoscale, $O(10\text{--}100)$ km, meanders and eddies in the Southern

Ocean. While the rich mesoscale structure of the ACC has been studied intensely, finer-scale variability along Southern Ocean fronts is less understood and observed.

Two of the most prominent fronts (Fig. 1) in the Southern Ocean are the Subantarctic and Polar Fronts (hereinafter, SAF and PF). Because of sparse data coverage in the Southern Ocean, altimetry-based frontal definitions have been developed; $\text{SSH}_{\text{SAF}} = -0.25$ m and $\text{SSH}_{\text{PF}} = -0.70$ m are updated values from Sallée et al. (2008). North of the SAF, water masses such as Subantarctic Mode Water (SAMW) and Antarctic Intermediate Water (AAIW) subduct along isopycnals at specific locations in the Southern Ocean, such as the Scotia Sea (Sallée et al. 2010). The subducted pools of SAMW and AAIW observed north of

⁸ Denotes content that is immediately available upon publication as open access.

Corresponding author: Katherine A. Adams, kate.adams@plymouth.ac.uk



This article is licensed under a Creative Commons Attribution 4.0 license (<http://creativecommons.org/licenses/by/4.0/>).

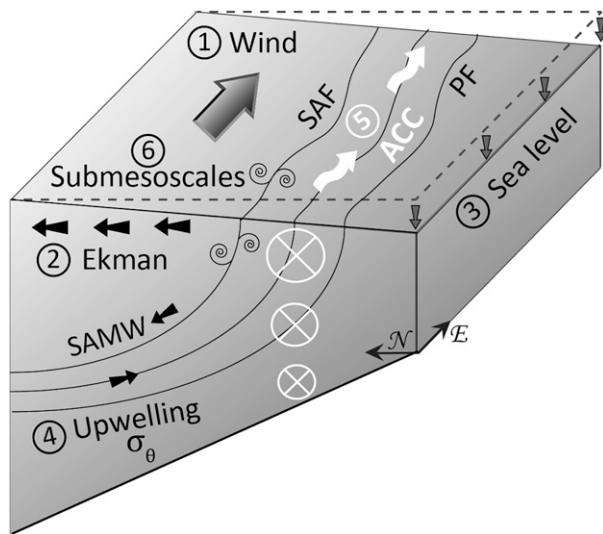


FIG. 1. Schematic of wind-driven upwelling in the Southern Ocean. The ACC, SAF, PF, and SAMW locations are labeled.

the ACC contain high levels of anthropogenic CO₂ (Sabine et al. 2004; Pardo et al. 2014) and heat (Frölicher et al. 2015). Currently, SAMW is thought to be transformed by air-sea buoyancy fluxes (Cerovecki et al. 2013) and subsequently mixed and subducted within AAIW, $\sigma_{\theta 27.2}$, to the South Atlantic (Sallée et al. 2010). In locations “upstream” of the subducted SAMW/AAIW pools, mode water transformation occurs in the mixed layer at the SAF and has climatic implications. The large-scale, $O(100\text{--}1000)$ km, physical processes, such as wind-driven and eddy-driven Ekman pumping, responsible for the subduction of heat and carbon in SAMW/AAIW pools have been discussed and documented (e.g., Sallée et al. 2010, 2012), but very little is known about subduction associated with smaller scales processes (Naveira Garabato et al. 2001).

A potentially important class of dynamics responsible for modulating the vertical exchange at fronts in the Southern Ocean occurs at the submesoscale, $O(1\text{--}10)$ km. The oceanic submesoscale is instrumental in extracting energy from density fronts and transferring the energy from mesoscale to submesoscale and dissipative scales (Thomas and Taylor 2010; Capet et al. 2008). The down-scale transfer of energy results in ageostrophic motions with large vertical velocities, $O(100)$ m day⁻¹ (Mahadevan and Tandon 2006; Capet et al. 2008; Thomas et al. 2008), capable of transporting heat and tracers across the base of the mixed layer. Where energetic submesoscale processes exist, the resulting vertical buoyancy fluxes may attain an importance equal to or greater than those forced by air-sea exchange.

The presence of fronts preconditions the mixed layer to the development of submesoscale processes, which

are characterized by $O(1)$ Rossby (Ro) and balanced Richardson (Ri_B) numbers (Thomas et al. 2008). Submesoscale dynamics are often associated with hydrodynamic instabilities including baroclinic mixed layer instability (MLI), symmetric instability (SI), inertial instability (II), and gravitational instability (GI) (Haine and Marshall 1998; Fox-Kemper et al. 2008; Thomas et al. 2008). These instabilities, with the exception of GI, grow at the expense of available potential energy associated with lateral density gradients (MLI) or thermal wind kinetic energy (II and SI). In each of these cases, instabilities are likely to develop at fronts and can significantly modify the mixed layer density structure (Boccaletti et al. 2007; Hosegood et al. 2008; Taylor and Ferrari 2009; Mahadevan et al. 2010). GI, conversely, is convectively driven and generated by unstable vertical stratification. Mixing associated with GI leads to deeper mixed layers, while MLI and SI results in restratification.

Sampling submesoscale processes presents challenges because of the complex dynamics of the mixed layer and the short spatiotemporal scales of variability, from hours to days and meters to kilometers. Very few submesoscale-resolving measurements have been made in the Southern Ocean (Rocha et al. 2016), though a recent modeling study has demonstrated the dependence of submesoscale vertical velocities on an energetic mesoscale eddy and strain field (Rosso et al. 2015). An energetic submesoscale is, therefore, expected in a region with high mesoscale eddy kinetic energy (EKE), such as the Scotia Sea, a mesoscale eddy hot spot (Frenger et al. 2015). Large, high-Ro meanders of the SAF and PF fronts (Fig. 2) are indicative of a highly energetic mesoscale field in the Scotia Sea region, suggesting the presence of an energetic submesoscale field.

Here we present novel observations of submesoscale variability in the Southern Ocean from the Surface Mixed Layer Evolution at Submesoscales (SMILES) project (<http://www.smiles-project.org>). SMILES aims to 1) characterize submesoscale dynamics and 2) evaluate the role of submesoscales in mode water transformation in the Scotia Sea using a combination of observations and models. The observational component of the SMILES project consists of a single research cruise to the Scotia Sea in May 2015, just before the austral winter. During a drifter-following cross-front survey, a northward meander of the SAF and PF (Fig. 2) separated from the ACC and formed a cold-core mesoscale eddy.

In this paper, we focus on the observed frontal circulation and submesoscale variability along the periphery of the newly formed eddy. Data sources and processing methods are described in section 2. Eddy formation, frontal circulation, cross-frontal variability, and water mass modification results from the drifter-following survey are presented in sections 3a–d, respectively.

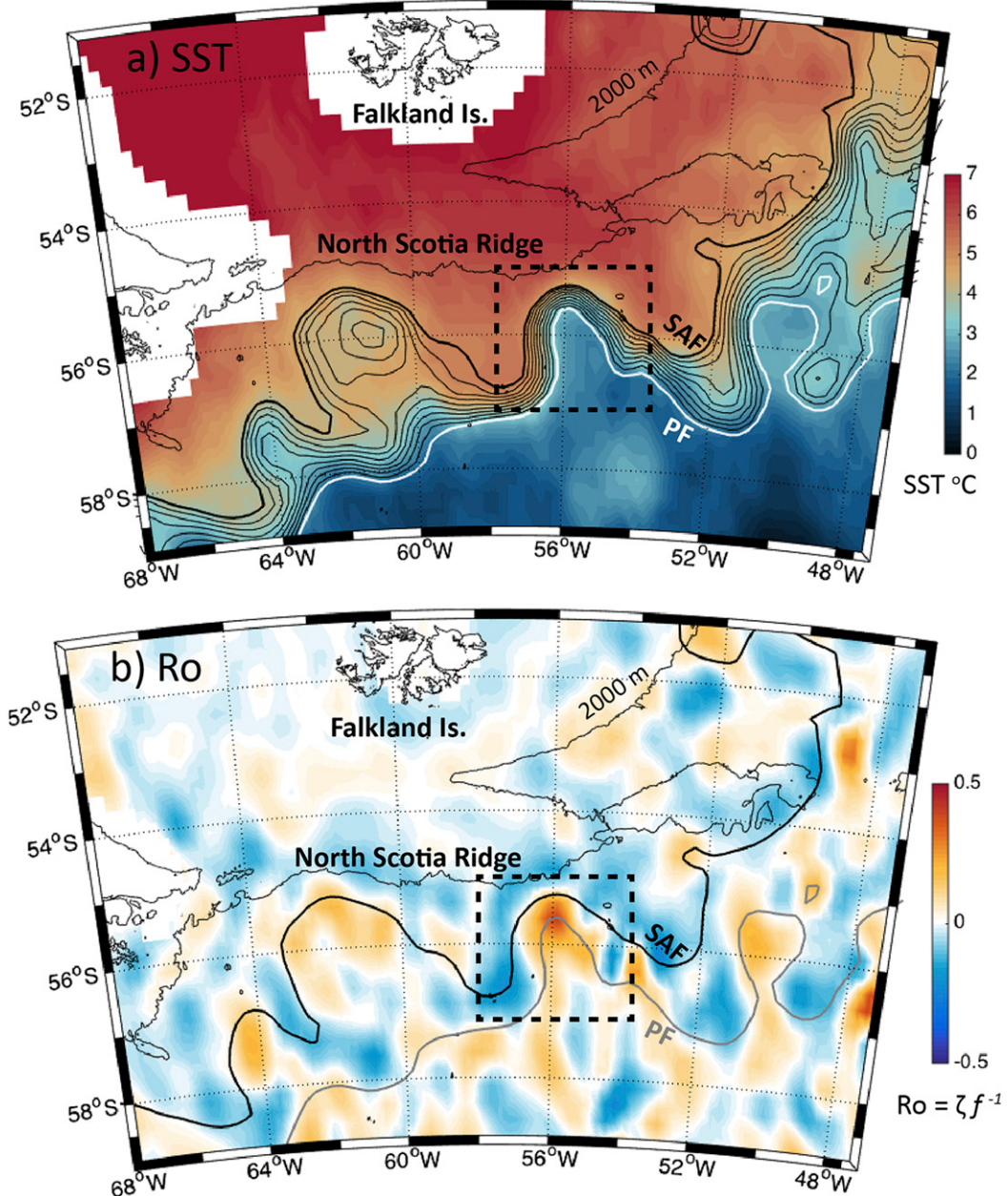


FIG. 2. (a) A northward meander (dashed box) of the ACC in the Scotia Sea, observed remotely on 20 April 2015, is characterized by sharp horizontal gradients of SST ($^{\circ}\text{C}$; color) and SSH (m; contours). (b) As in (a), but for vorticity Rossby number (color) calculated from altimetry-derived geostrophic surface currents. SSH contours corresponding to the SAF (-0.25 m) and PF (-0.70 m) fronts define the northern and southern edges of the meander, respectively. The 2000-m isobath from the General Bathymetric Chart of the Oceans dataset outlines the North Scotia Ridge, the northern boundary of the Scotia Sea.

Downloaded from http://journals.ametsoc.org/jpo/article-pdf/47/7/1737/481061/jpo-d-16-0266_1.pdf by Dhruv Bawada on 29 October 2020

Section 4 presents an estimation of vertical velocity and a submesoscale instability analysis with implications for mode water modification. In section 5, results are summarized and the implications of submesoscale processes during eddy formation in the Scotia Sea are discussed.

2. Data sources and methods

a. Ship-based data sources

The field component of the SMILES project consisted of a Scotia Sea research cruise, 22 April to 21 May 2015, performed aboard the British Antarctic Survey RRS

James Clark Ross (JCR). Seasoar, a winged and towed body equipped with a Sea-Bird Scientific SBE 911, collected temperature, conductivity, and pressure measurements at 16 Hz. Seasoar data are collected in a sawtooth pattern (Fig. 3) at 8 kt ($\sim 4 \text{ m s}^{-1}$) with a horizontal spacing between apogees of 2 km for 200-m dives. Temperature T and salinity S variables were binned to 0.5 dbar intervals. Binned data were gridded using a two-dimensional Gaussian interpolation scheme (Barnes 1964) with regular spacing, 0.5 km horizontal and 1 m vertical, and decorrelation radii of 1 km and 2 m (Fig. 3c).

Horizontal currents were collected in 8-m-depth bins over 22–600 m of the water column by the ship-mounted Teledyne Oceanscience 75-kHz acoustic Doppler current profiler (ADCP). The collected data were cleaned, corrected for ship speed and heading, and ensemble averaged to 150-s bins using Common Ocean Data Access System (CODAS) processing tools. North and east velocity components from 30 to 200 m were interpolated to the same grid as the Seasoar data, then rotated into alongfront and cross-front velocity components using the drifter trajectories as explained below. Error velocities reported from the ADCP processing software are used as estimates of velocity uncertainty in the calculations in section 4a.

b. Drogued drifters

A triplet of drogued drifters was used in the survey to estimate horizontal water velocities at 50-m depth. The drifters consisted of a sealed buoy with GPS and satellite communications, a “holey sock” drogue 10 m long and 90 cm in diameter centered at 50-m depth, and a 3.5 mm Dyneema line. This design provided a drag area ratio of 44, which is accurate to follow water parcels to within 1 cm s^{-1} (Sybrandy et al. 2009). Drifter location updates were received at 10-min intervals.

The drifters were released in the northern portion of the meander just south of the maximum jet velocity and temperature gradient (Fig. 3a) for the first Seasoar leg of the survey. In a current of $\sim 1.25 \text{ m s}^{-1}$, the 3-min separation of the drifter releases yields an initial alongfront drifter separation of $\sim 225 \text{ m}$. The trajectory of the first drifter released, D16, was chosen to define the alongfront direction in the survey analysis, θ_{along} (Table 1). The alongfront reference frame assumes the drifter maintains its position in the front and jet, which is shown in Fig. 4. The closest drifter crossing in time and space of each Seasoar leg defines the center of each section, with cross-frontal distance increasing outward, or away, from the eddy center. Each leg was rotated to a cross-front heading θ_{cross} , defined as the orthogonal direction to θ_{along} for each respective Seasoar leg (Table 1). Similarly, measured horizontal water velocities were rotated into alongfront and cross-front components for each leg.

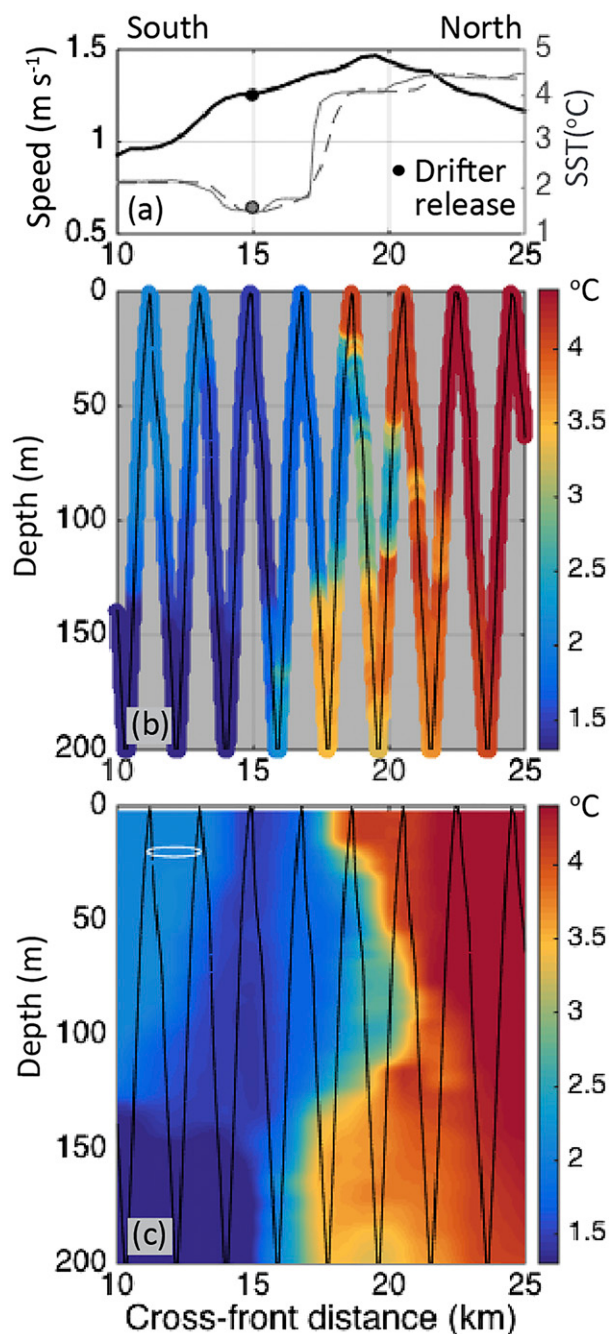


FIG. 3. (a) Measured jet speed (m s^{-1}) at 50-m depth and underway SST ($^{\circ}\text{C}$) at 4-m depth during the first Seasoar leg in survey. Gridded Seasoar temperature at 5-m depth is dashed. Drifters were released in the cold filament (1.56°C) with jet speed $\sim 1.25 \text{ m s}^{-1}$, approximately 15 km from the start of the Seasoar leg. (b) Temperature data binned into 0.5-m intervals for the first Seasoar leg. (c) As in (b), but for gridded temperature data with the interpolation window $2 \text{ km} \times 4 \text{ m}$ shown as an ellipse (white). The location of Seasoar measurements in (b) and (c) are black.

TABLE 1. True drifter and Seasoor leg headings. The alongfront direction θ_{along} is defined by the drifter D16 trajectory. The cross-front direction θ_{cross} is $\theta_{\text{along}} - 90^\circ$. The mean true heading of Seasoor legs θ_{leg} are calculated with cross-front distance increasing away from the eddy center. Legs are projected onto a cross-frontal axis through a rotation of $\theta_{\text{rot}} = \theta_{\text{cross}} - \theta_{\text{leg}}$. The axis projection alters the horizontal spacing of survey measurements by the multiplication factor $\cos(\theta_{\text{rot}})$. Legs correspond to section labels in Fig. 5.

Leg	θ_{along}	θ_{cross}	θ_{leg}	θ_{rot}	$\cos(\theta_{\text{rot}})$
13 (N)	74.5	344.5	340.4	4.1	1.00
14	83.7	353.7	344.1	9.6	0.99
17	109.5	19.5	343.7	35.8	0.81
19	143.3	53.4	42.1	11.2	0.98
20 (NE)	157.6	67.6	52.8	14.8	0.97
21	179.2	89.3	51.2	38.1	0.79
22	200.5	110.5	101.1	9.4	0.99
23	200.5	110.5	127.2	-16.7	0.96
24	202.1	112.1	119.3	-7.1	0.99
25	206.4	116.4	131.9	-15.5	0.96
26 (E)	209.5	119.5	132.9	-13.4	0.97
27	215.7	125.7	137.7	-12.1	0.98
28	216.0	126.0	121.9	4.1	1.00
29 (SE)	214.8	124.8	119.4	5.4	1.00
32	232.1	142.1	169.6	-27.5	0.89
33	240.7	150.7	170.2	-19.4	0.94
35 (S)	284.2	194.2	179.9	14.3	0.97
36	296.8	206.8	179.4	27.4	0.89
37	296.5	206.5	179.8	26.7	0.89
38	305.8	215.8	179.4	36.3	0.81
39	309.2	219.2	180.1	39.1	0.78
40	311.5	221.5	189.8	31.7	0.85
41	26.0	296.0	325.4	-29.4	0.87
43	53.1	323.1	1.7	38.6	0.78
44	71.2	341.2	345.1	-3.9	1.00

c. Remote data sources

Satellite sea surface temperature (SST) and SSH data were used for mesoscale frontal and eddy detection during the cruise and the analysis. Both datasets are available daily on a 0.25° grid. Figure 2 is an example of the remote sensing data available during the SMILES cruise. The daily, gridded optimally interpolated microwave SST data (OISST) was obtained from Remote Sensing Systems (REMSS; <http://www.remss.com>). SSH, or absolute dynamic topography, and altimetrically derived geostrophic surface current data were downloaded from AVISO CNES (www.aviso.altimetry.fr; Pujol et al. 2016). SAF and PF positions are defined using SSH contours of -0.25 and -0.7 m, respectively, updated from the definitions in Sallée et al. (2008).

3. Results

a. Eddy formation

A northward meander of the SAF and PF developed along the ACC (Fig. 2) in late April 2015. This mesoscale,

$O(100)$ km, feature characterized by meridional changes of 4°C SST and 0.5-m SSH over 50 km, formed just south of the North Scotia Ridge. Antarctic surface water, $<2^\circ\text{C}$ south of the PF (Orsi et al. 1995), is observed in the center of the meander. The vorticity Rossby number, $\text{Ro} = \zeta f^{-1}$, of the meander as calculated from altimetry-derived geostrophic surface currents from 20 April is ~ 0.4 . This moderate Ro value based on coarse altimetry data does not account for ageostrophic contributions from curvature (e.g., cyclogeostrophic flow). Although the moderate Ro estimate is high compared to previous submesoscale-focused process studies, for example, $\text{Ro} \sim 0.1$ in the North Pacific (Hosegood et al. 2013), it is not uncommon for this region.

A triplet of drogued drifters released in the northwest sector of the meander on 8 May 2015 at 2000 UTC was followed with the RRS *JCR* while towing the Seasoor CTD perpendicular to the drifter trajectories. The daily progression of SST, SSH, drifter trajectories, and the ship track are presented in Fig. 4 for 8–12 May 2015. At the time of the drifter release, 18 days after the SST and SSH observations presented in Fig. 2, the meander had sharpened yet remained tethered to the ACC as observed by SST and SSH fields (Fig. 4a). During the survey, the drifters initially traveled east (Fig. 4b) and southeast (Fig. 4c) around the meander and remarkably continued along a cyclonic trajectory precisely as the meander separated from the ACC and formed a cold closed-core eddy (Figs. 4c–e). Initially, the cyclonic eddy measured approximately 120 km in diameter with a dynamic height anomaly of 0.5 m (-0.2 to -0.7 m SSH). After the eddy formed (Fig. 4e), the SAF and PF returned to a zonal orientation south of the eddy. Hereafter, the meander/eddy feature will be referred to as an eddy for the duration of the Seasoor survey.

The Seasoor survey, shown as the ship track in Fig. 4, consisted of 25 sections around the edge of the eddy ranging from 25 to 40 km in length. Maps of 10-m-depth temperature and salinity from these 25 sections are presented in Figs. 5a and 5b. The beginning northern sector of the survey is characterized by sharp temperature and salinity fronts (2°C , 0.2 psu in 2 km at 4 m depth) with warm, salty water outside and cold, fresh waters inside the eddy. A region characterized by a loss of temperature and salinity frontal integrity is observed along the southern portion of the survey. The repeat observation of temperature and salinity intrusions in consecutive sections suggests the presence of a three-dimensional structure such as a submesoscale streamer or filament, only a few kilometers across, in the newly formed southern eddy sector. Note that the filaments occur in a region that was previously an open meander characterized by weak lateral gradients in temperature and salinity.

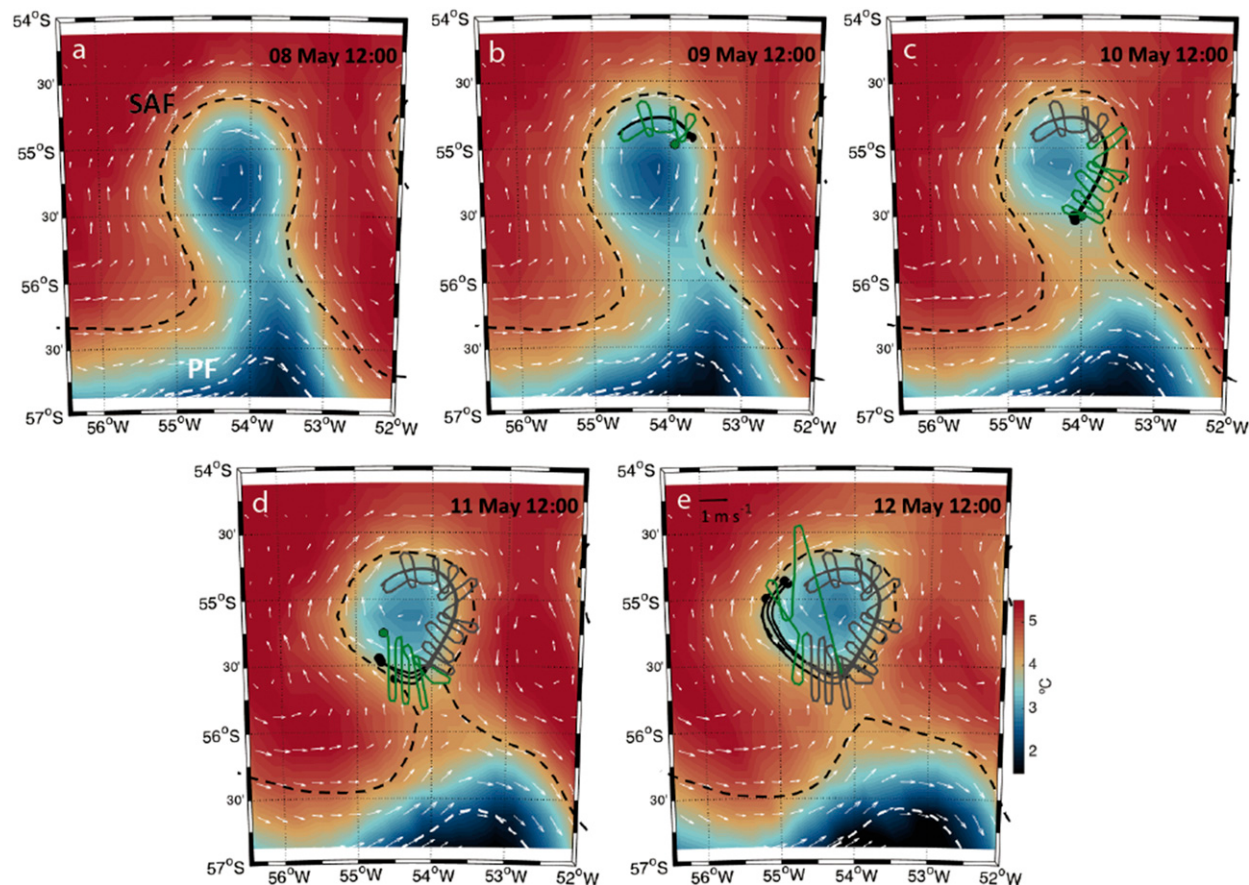


FIG. 4. Daily snapshots of microwave SST (REMSS) and altimetric geostrophic surface current vectors (AVISO) for 8–12 May 2015 capturing the formation of a mesoscale eddy from a northward meander along the ACC in the Scotia Sea (Fig. 2). A drifter triplet (black) was released on 8 May at 2000 UTC in the northwestern sector of the meander and followed while towing the Seasor with the RRS *JCR* (green). Positions of the SAF and PF, defined by the -0.25-m and -0.70-m SSH contours, are shown in black and white dashed lines, respectively.

Horizontal water velocities measured at 50-m depth are included in Figs. 5c and 5d where the alongfront and cross-front components are determined relative to a drifter trajectory direction (Table 1) for each Seasor section. A $\sim 70\%$ decrease ($1.5\text{--}0.4\text{ m s}^{-1}$) in drifter and alongfront water velocities is observed from north to south. Geostrophic surface velocity vectors (Fig. 4) also show weaker currents in the southern portion of the eddy compared to the north. A sign change in cross-frontal velocities on either side of the drifters indicates diffluent flow during the majority of the survey with confluent cross-frontal flow in the southern portion of the survey.

The ageostrophic component of the curved flow around the eddy can be estimated from the along-frontal velocities by comparing the centripetal acceleration term with the Coriolis acceleration, $C = u(Rf)^{-1}$. Assuming an eddy radius $R = 50\text{ km}$, C is maximum (0.25) along the northern portion of the survey and minimum (0.10) in the southern eddy sector. This indicates

a larger cyclogeostrophic component to the flow in the north.

Wind forcing during the Seasor survey was unusually calm for April in the Southern Ocean with wind speeds $< 10\text{ m s}^{-1}$ and winds from southeast to northwest rather than the expected westerlies.

A partial infrared SST image of the eddy was captured during the Seasor survey by an AVHRR sensor aboard the *MetOp-A* satellite on 11 May 2015 at 1242 UTC (Fig. 6a). The high-resolution (1 km) SST data show strong gradients along the northern eddy boundary and weaker gradients to the southeast, similar to Fig. 5a. Unfortunately, clouds mask the southern and western sectors of the eddy. The ship's underway temperature data at 4-m depth are overlaid on the infrared SST data in Fig. 6b. The noticeable offset in temperatures is due to the northward movement of the eddy in the 2.5 days between the beginning of the survey and the satellite measurements. The ship's temperature data are also plotted atop optimally

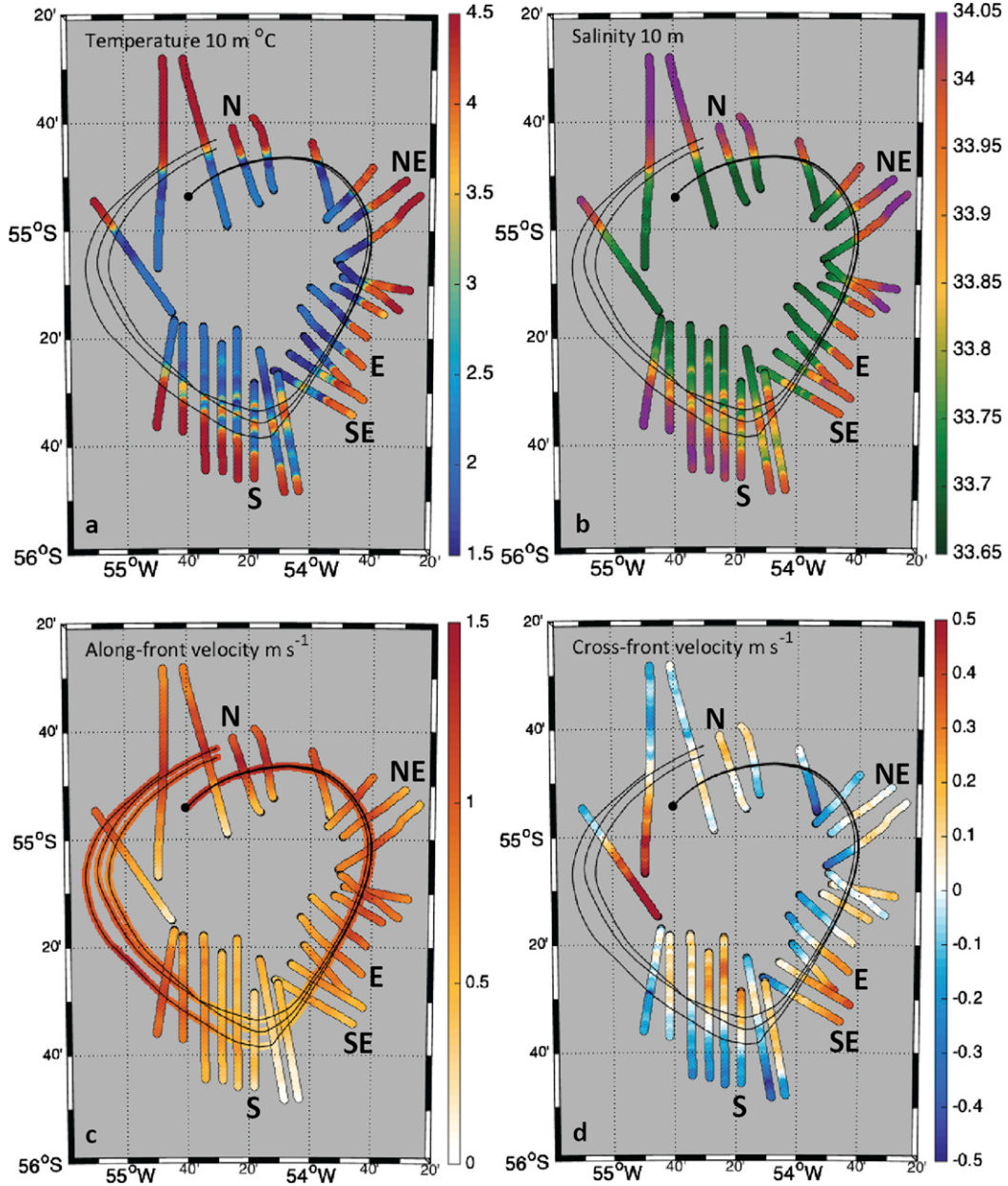


FIG. 5. Maps of 10-m depth (a) temperature and (b) salinity and 50-m depth (c) alongfront and (d) cross-front velocity measurements from the drifter-following Seasor survey introduced in Fig. 4. A circle marks the starting position of the cyclonic survey. Drifter triplet tracks are shown in black except in (c), where drifter speed is also in color. Positive alongfront velocities indicate a cyclonic (clockwise) direction where positive cross-front velocities indicate flow out of the eddy. Labeled Seasor legs, indicating the approximate location in the survey, are presented in Fig. 7.

Downloaded from http://journals.ametsoc.org/jpo/article-pdf/47/7/1743/481061/jpo-d-16-0266_1.pdf by Dhruv Bawada on 29 October 2020

interpolated microwave SST data for 11 May 2015. The eddy boundary, defined by the 3°C isotherm in Figs. 6a and 6c, is drastically different between the 1-km infrared and coarser microwave SST data.

b. Cross-frontal variability

Vertical cross sections of potential density anomaly (σ_0 , kg m^{-3}), temperature ($^{\circ}\text{C}$), salinity, and horizontal

water velocities (m s^{-1}) are presented in Fig. 7 for the Seasor legs labeled in Fig. 5. The five sections span approximately 2 days and 180° of heading of the drifter-following survey. Each section is referenced in a similar manner with respect to the front; the left (right)-hand side of the sections will be referred to as inner (outer) with negative (positive) cross-frontal distance. Since the sections are centered using the drifter trajectories, a

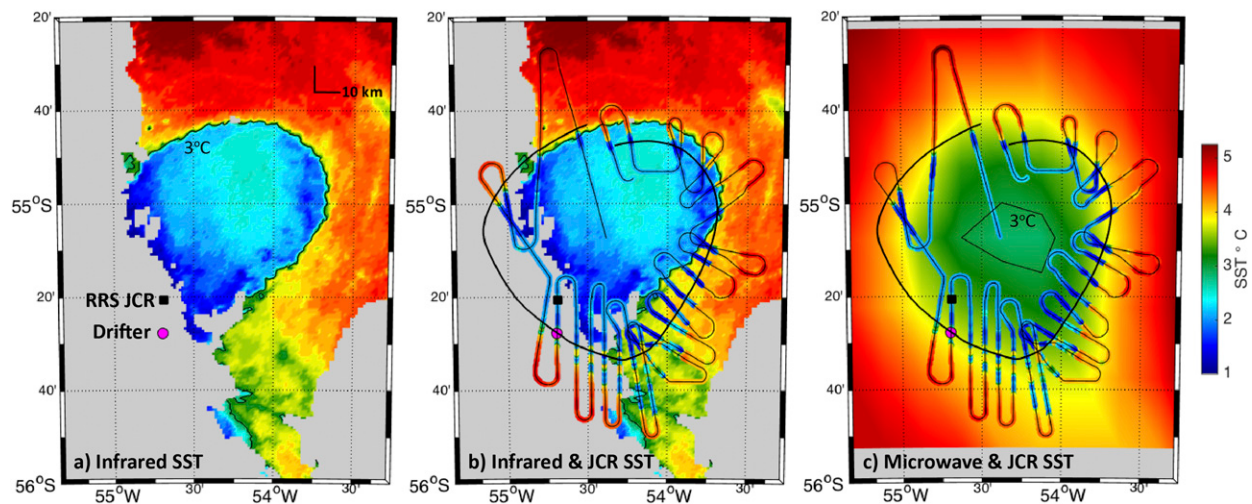


FIG. 6. (a) Level 2 infrared SST measured at 11 May 2015 at 1242 UTC by an AVHRR sensor with 1-km horizontal resolution on the *MetOp-A* satellite as the drifters (circles) and the RRS *JCR* (squares) were completing the southwest sector of the Seasoor survey. (b) *JCR* underway temperature data measured during the survey at 4-m depth and 40-m horizontal resolution overlaid on (a). A drifter track (black) is included. (c) As in (b), but overlaid on microwave SST (OISST; www.remss.com). The 3°C isotherm (black) outlines the eddy center in (a) and the eddy edge in (c).

cross-frontal distance of zero is not an explicit definition of the frontal center with respect to density.

In leg N, σ_θ increases laterally away from the eddy core except for a dense filament ~ 5 km in width located in the center of the leg (Fig. 7a). The filament, with temperatures $<1.6^\circ\text{C}$, is observed between two outcropping isopycnals with a potential density anomaly of 27.0 kg m^{-3} (hereinafter σ_{027}). The inner density gradient, 0.09 kg m^{-3} in 5 km, is nearly twice the magnitude of the warm, outer density front, 0.04 kg m^{-3} in 5 km. In leg E, the σ_{027} is observed subsurface. By leg S, the depth of the σ_{027} is much shallower on the inner side of the leg.

Mixed layer depth (MLD), defined as the level of a 0.01 kg m^{-3} density increase from 5-m depth, is included in Fig. 7a. This strict MLD definition was chosen to highlight the lateral density gradients in the current dataset. Values of MLD are $O(100)$ m for most of leg N. In each leg, the mixed layer is shallowest within the density fronts (<50 m) and deepest within the dense filament (130 m). The MLD shoals similarly to σ_{027} in leg S, suggestive of restratification of the inner front along the newly formed sector of the eddy. The shallower MLD may be the result of temporal variability, for example, restratification from submesoscale instabilities, or spatial variability.

Temperature and salinity fields vary similarly across the sections (Figs. 7b and 7c) because of strong density compensation, a characteristic of ACC fronts. In leg N, the warm, salty outer region lies adjacent to a cold, dense filament at a cross-frontal distance of 0 km. Leg E, in the east sector of the survey, contains a small subsurface

cold water intrusion at 120-m depth and 10-km cross-front distance. Intrusions of cold freshwater on the outer side and warm, salty water on the inner side are observed in all legs collected in the east and southeast sectors of the survey. In leg SE, the intrusion is larger in vertical and horizontal extent and outcropped. In leg S a loss of frontal integrity is observed compared to the well-organized, separated cold-fresh inner and warm-salty outer regions present in leg N.

Vertical cross sections of alongfront and cross-front velocities (Figs. 7d and 7e) show a strong barotropic component to the flow. Trends throughout the survey agree with the 50-m maps in Figs. 5c and 5d. Alongfront velocities decrease whereas cross-front velocities switch from confluent to diffluent from legs N to S.

c. Frontal circulation

The frontal circulation at the center of each Seasoor leg can be described using the collocated drifter and horizontal water velocity datasets. As shown in Fig. 8a, the drifter and alongfront water velocities at 50-m depth are in strong agreement. Drifters initially deployed in the northern sector of the cyclonic eddy decelerated around the eastern side toward the southern sector where the alongfront velocity is minimum, after which the drifters accelerated around the western edge. Similar trends were observed in the measured alongfront velocity. The cross-frontal gradient of cross-frontal velocity was positive (diffluent) during the alongfront deceleration and negative (confluent) during the alongfront acceleration, as shown in Fig. 8b.

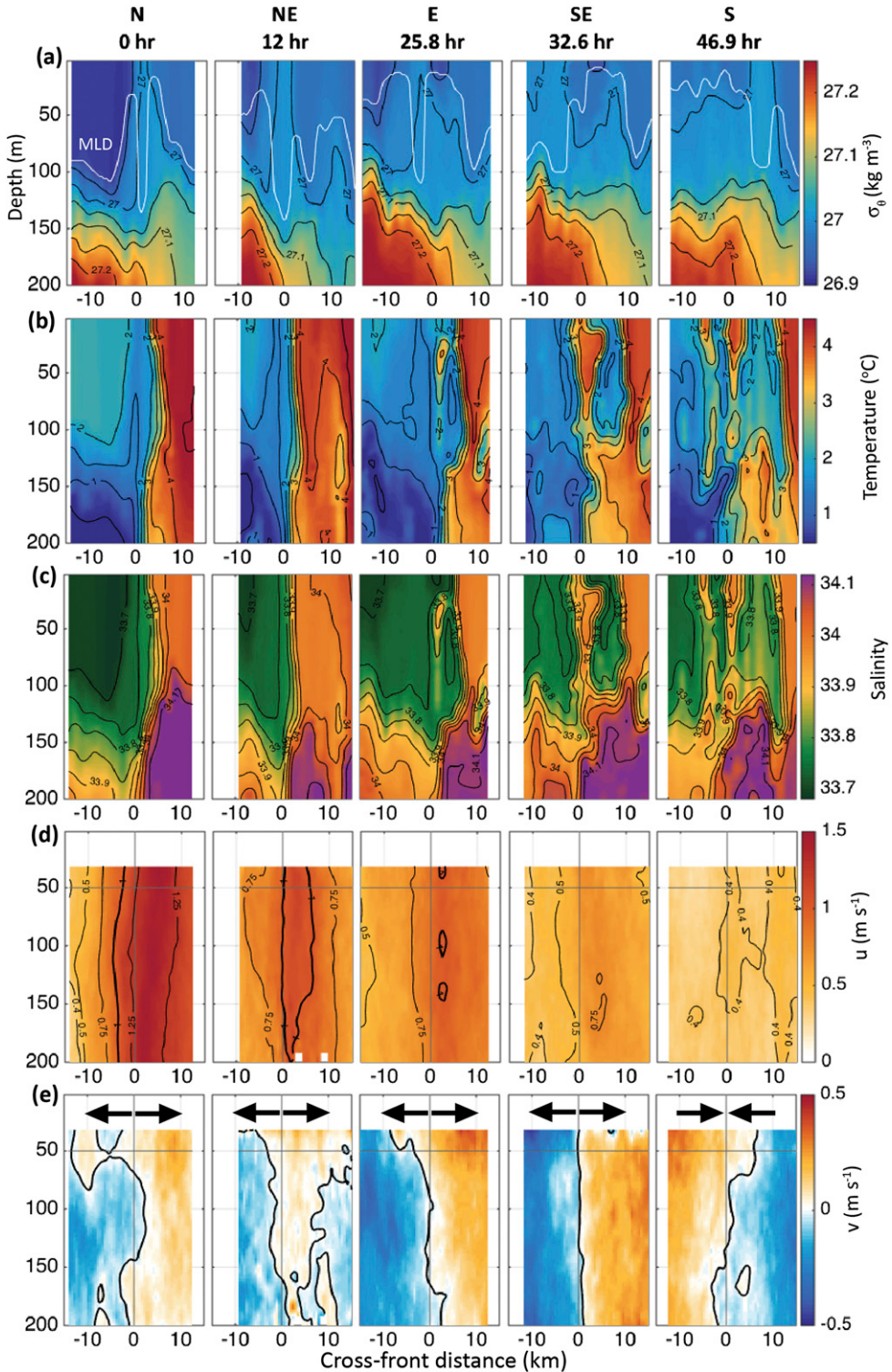


FIG. 7. Vertical cross-front sections of (a) potential density anomaly (kg m^{-3}), (b) temperature ($^{\circ}\text{C}$), (c) salinity, (d) alongfront velocity, and (e) cross-front velocity for SeaSoar legs N, NE, E, SE, and S. The start time since the start of leg N is reported above (a) in hours. Sections are oriented such that cross-front distance increases away from the meander and eddy center. MLD, defined as a 0.01 kg m^{-3} density difference from the surface, is white in (a). The drifter location during each leg is at cross-front distance = 0 and depth = 50 m, shown at the intersection of gray lines in (c) and (d).

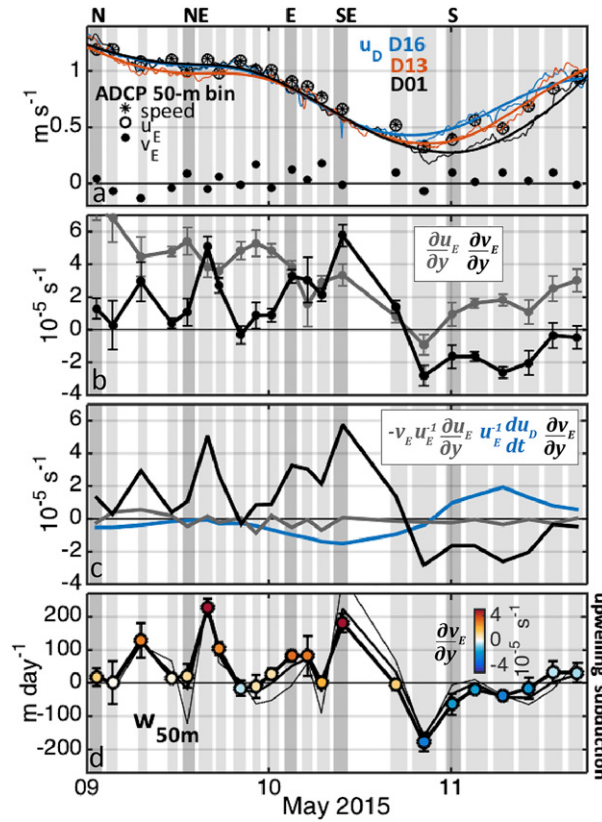


FIG. 8. (a) Time series of alongfront drifter velocity u_D^D (m s^{-1}) for the three drifters released and followed during the Seasoor survey from 9 to 12 May 2015. Alongfront x and cross-front y water velocity components, u_E and v_E , measured within 1 km of the frontal center are shown for the drifter drogue depth of 50 m. Water speed (*) is also included. (b) Cross-front gradients of u_E (gray) and v_E (black) at 50-m depth and averaged ± 1 km across the front. Negative $\partial \bar{v}_E / \partial y$ (black) indicates confluent flow. Error bars indicate uncertainty of the ADCP measurements. (c) Estimation of terms in Eq. (9) after making steady-state assumption. (d) Vertical velocity at the drogue depth of 50 m, w_{50m} (m day^{-1}), with $\partial \bar{v}_E / \partial y$ (s^{-1}), from (b) shown in color. Error velocities of the ADCP are propagated through the calculation of w and are shown as error bars. Additional estimates of w are included for the slab (black) and linear (gray) extrapolations of u_E and v_E to the surface. Vertical velocities and $\partial \bar{v}_E / \partial y < 0$ indicate subduction and confluence, respectively. The duration of Seasoor legs is shaded in each panel.

4. Analysis

a. Estimation of vertical velocity

Vertical velocities w were not directly measured in the SMILES Seasoor survey. However, the collocated drifter and ADCP datasets allow for the following mathematical framework, which yields a solvable expression for w at a specific depth and a cross-frontal location in each Seasoor leg. Assumptions made in the following derivation are tested in the appendix.

Let $\mathbf{x}_D(t)$ and $\mathbf{u}_D(t)$ be the measured drifter position and velocity vectors at time t , where

$$\left(\frac{dx_D}{dt}, \frac{dy_D}{dt} \right) = [u_D(t), v_D(t)]. \quad (1)$$

Let $\mathbf{u}_E(x, y, z, t)$ be the Eulerian fluid velocity. Assume that the drifter moves with the vertically averaged Eulerian velocity at the horizontal location of the drogue from depth z_1 to z_2 :

$$\frac{d\mathbf{u}_D}{dt} = \frac{d}{dt} \{ \bar{\mathbf{u}}_E[x_D(t), y_D(t), t] \}, \quad (2)$$

where

$$\bar{\mathbf{u}}_E \equiv \frac{1}{z_1 - z_2} \int_{z_2}^{z_1} \mathbf{u}_E dz. \quad (3)$$

Here we set $z_1 = 0$ at the surface and $z_2 = 50$ m as the drifter drogue depth. This assumes the drogued drifter is moving with the depth-integrated Eulerian velocity in the top 50 m of the water column. Justification for this assumption is presented in the appendix. Expanding the derivative in (2),

$$\frac{d\mathbf{u}_D}{dt} = \frac{\partial \bar{\mathbf{u}}_E}{\partial t} + \frac{dx_D}{dt} \frac{\partial \bar{\mathbf{u}}_E}{\partial x} + \frac{dy_D}{dt} \frac{\partial \bar{\mathbf{u}}_E}{\partial y} = \frac{\partial \bar{\mathbf{u}}_E}{\partial t} + \bar{\mathbf{u}}_E \cdot \nabla_H \bar{\mathbf{u}}_E. \quad (4)$$

where $\nabla_H \equiv (\partial/\partial x, \partial/\partial y)$. From continuity, $\nabla \cdot \mathbf{u}_E \equiv 0$, hence $\nabla \cdot \bar{\mathbf{u}}_E = 0$ for constant z_1 and z_2 ,

$$\frac{\partial \bar{u}_E}{\partial x} + \frac{\partial \bar{v}_E}{\partial y} + \frac{w_E(x_D, y_D, z_1, t) - w_E(x_D, y_D, z_2, t)}{z_1 - z_2} = 0. \quad (5)$$

From (4), the rate of change of the alongfront drifter velocity is

$$\frac{du_D}{dt} = \frac{\partial \bar{u}_E}{\partial t} + \bar{u}_E \frac{\partial \bar{u}_E}{\partial x} + \bar{v}_E \frac{\partial \bar{u}_E}{\partial y} \quad (6)$$

while (5) gives

$$\frac{\partial \bar{u}_E}{\partial x} = -\frac{\partial \bar{v}_E}{\partial y} - \frac{w_E|_{z_1} - w_E|_{z_2}}{z_1 - z_2}. \quad (7)$$

Substituting (7) in (6) gives

$$\frac{du_D}{dt} = \frac{\partial \bar{u}_E}{\partial t} - \bar{u}_E \frac{\partial \bar{v}_E}{\partial y} - \bar{u}_E \frac{w_E|_{z_1} - w_E|_{z_2}}{z_1 - z_2} + \bar{v}_E \frac{\partial \bar{u}_E}{\partial y}. \quad (8)$$

Rearranging (8) yields an expression for the difference of vertical velocity from z_1 to z_2 :

$$\begin{aligned} w_E|_{z_1} - w_E|_{z_2} \\ = (z_1 - z_2) \left(-\frac{1}{\bar{u}_E} \frac{du_D}{dt} + \frac{1}{\bar{u}_E} \frac{\partial \bar{u}_E}{\partial t} - \frac{\partial \bar{v}_E}{\partial y} + \frac{\bar{v}_E}{\bar{u}_E} \frac{\partial \bar{u}_E}{\partial y} \right). \end{aligned} \quad (9)$$

An expression for w_E at the drogue depth z_2 is obtained by setting $w_E(z_1 = 0) = 0$,

$$w_E|_{z_2} = z_2 \left(\frac{1}{\bar{u}_E} \frac{du_D}{dt} - \frac{1}{\bar{u}_E} \frac{\partial \bar{u}_E}{\partial t} + \frac{\partial \bar{v}_E}{\partial y} - \frac{\bar{v}_E}{\bar{u}_E} \frac{\partial \bar{u}_E}{\partial y} \right). \quad (10)$$

We can make a steady-state assumption,

$$\frac{\partial \bar{u}_E}{\partial t} \ll \frac{du_D}{dt}, \quad (11)$$

if local accelerations are smaller than drifter accelerations on time scales greater than a day, the filtering window of the drifter velocities. This is tested in the appendix, making use of ship track intersections during the survey. We then have an expression,

$$w_E|_{z_2} = z_2 \left(\frac{1}{\bar{u}_E} \frac{du_D}{dt} + \frac{\partial \bar{v}_E}{\partial y} - \frac{\bar{v}_E}{\bar{u}_E} \frac{\partial \bar{u}_E}{\partial y} \right), \quad (12)$$

that allows for the calculation of vertical velocity in the center of each Seasoor leg at z_2 , the drifter drogue depth of 50 m (Fig. 8d). Velocity components \bar{u}_E and \bar{v}_E are first calculated by averaging velocities from the first good ADCP bin, 30 m, to 50 m, as in Fig. 8a. Extrapolations to the surface are used to approximate \bar{u}_E from $z = 0$ –50 m, as detailed in the appendix. The cross-frontal velocity gradients, $\partial \bar{u}_E / \partial y$ and $\partial \bar{v}_E / \partial y$, are averaged ± 1 km from the center of each Seasoor leg (Fig. 8b). Error velocities reported by the ADCP processing and propagated through the w calculation are shown as error bars in Fig. 8d.

Vertical velocities calculated from (12) are presented in Fig. 8d. Upwelling velocities are calculated during the north, northeast, and east sectors of the survey, when diffluent cross-front flow and drifter deceleration is observed. Subduction is indicated in the southern survey sector when drifters accelerated. There is a strong dependence on $\partial \bar{v}_E / \partial y$ in our calculation, indicating the cross-frontal flow is driving the vertical circulation. The estimated magnitudes of $w_E|_{50\text{m}}$, $O(100)$ m day $^{-1}$, are similar to reported values for submesoscale processes; however, we cannot discern the relative contributions of mesoscale and submesoscale vertical motions here.

b. Submesoscale instabilities

Although direct measurements of submesoscale instabilities were not made during the Seasoor survey, it is

possible to diagnose whether conditions were favorable for submesoscale instability growth and which specific instabilities were possible (Thomas et al. 2013; Thompson et al. 2016). First, instability development is favored when Ertel potential vorticity (EPV),

$$\text{EPV} = \boldsymbol{\omega}_a \cdot \nabla b = (\mathbf{f} + \nabla \times \mathbf{u}) \cdot \nabla b, \quad (13)$$

is the opposite sign of f (Hoskins 1974; Haine and Marshall 1998; Thomas et al. 2008); the absolute vorticity $\boldsymbol{\omega}_a$ is the sum of planetary and relative vorticity and buoyancy is $b = -g\rho'p_0^{-1}$. The perturbation density ρ' is the measured density ρ minus the average leg density ρ_0 . This EPV criterion has been shown to hold even in flow regimes where ageostrophic processes such as down-front winds (Thomas and Taylor 2010; Thomas et al. 2013), inertial shear (Thomas et al. 2016), and surface-wave-driven shear (Haney et al. 2015) drive symmetric instability.

Expanding (13) gives

$$\text{EPV} = (w_y - v_z)b_x + (u_z - w_x)b_y + [f + (v_x - u_y)]b_z, \quad (14)$$

where subscripts indicate a partial derivative and x and y are the alongfront and cross-front directions. Neglecting ∂x terms in (14) assumes alongfront gradients \ll cross-front gradients. This simplification yields,

$$\text{EPV} \simeq (f - u_y)b_z + u_z b_y, \quad (15)$$

an approximation for EPV dependent on cross-front and vertical gradients in the alongfront velocity and buoyancy. The two-dimensional approximation of EPV (15) is shown in Fig. 9 below the cross-frontal buoyancy gradient at 10 m depth, which identifies density fronts in each leg. Regions with positive EPV ($f < 0$) are favorable for the instabilities described above and are observed on either side of the lateral buoyancy gradients, or fronts, and mostly above the MLD. The band of negative EPV in each leg is stable to instabilities because of the strong vertical stratification b_z of the ML base.

The EPV calculation in (15), expressed in the local Cartesian coordinate system for each Seasoor leg, neglects effects due to the curved flow around the eddy. We now consider EPV in cylindrical coordinates (Shakespeare 2016),

$$\text{EPV}_{\text{cyl}} = (f + u_{\theta_r} + u_\theta R^{-1})b_z - u_{\theta_z}b_r, \quad (16)$$

where R is the curvature of the flow and the azimuthal velocity u_θ is negative in a clockwise (cyclonic) rotational sense. The curvature term $u_\theta R^{-1}b_z$ is negative in stably stratified conditions ($b_z > 0$) and therefore will decrease EPV from the estimate in (15). The EPV calculation

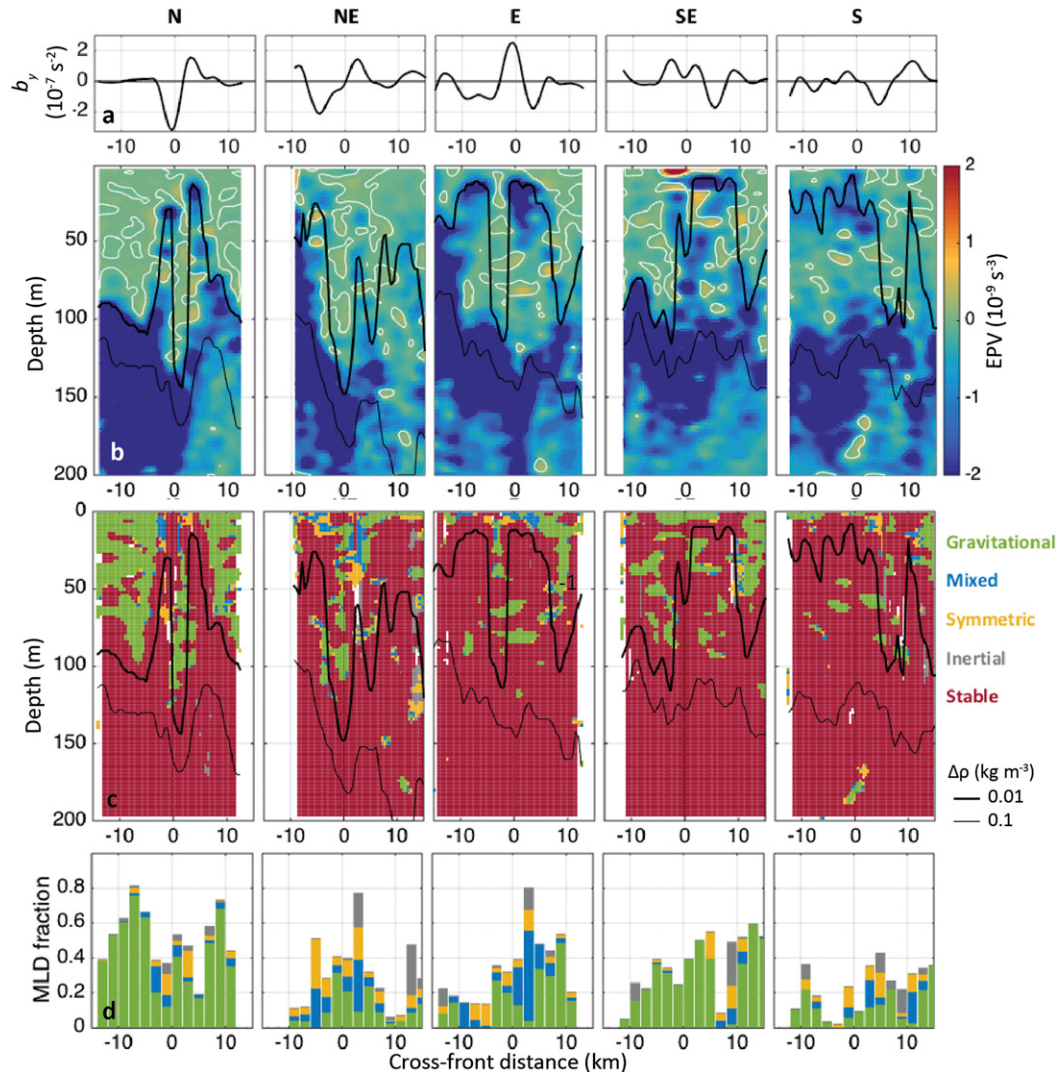


FIG. 9. (a) Cross-front buoyancy gradient b_y (s^{-2}) calculated at 10-m water depth for Seasor legs N, NE, E, SE, and S. Legs are oriented with the inside of the meander and eddy on the left-hand side of each panel. (b) A two-dimensional estimate of Ertel potential vorticity (s^{-3}) is shown with the zero contour in white and the MLD, defined as a 0.01 (0.1) kg m^{-3} density difference from the surface, as a thick (thin) black line. (c) Submesoscale instability analysis results based on the Ri_B criteria. (d) Instances of instabilities identified in (c) shown as a fraction of the 0.01 kg m^{-3} density difference MLD.

was repeated using (16) for legs N, NE, E, SE, and S using an eddy radius $R = 50 \text{ km}$ (not shown). The average percent difference in leg N (leg S) is 23% (7%); however, the inclusion of the curvature term has an indiscernible change on the EPV panels in Fig. 9b. The number of locations with $\text{EPV} > 0$ decreased by 0.75% (leg N) to 0.15% (leg S). Therefore, the total EPV is slightly lower when curvature effects are considered. This could result in a slight overestimation in the number of locations identified as favorable for inertial and symmetric instabilities below.

For regions where EPV is positive ($f < 0$), specific submesoscale instabilities can be identified using the

balanced Richardson number $\text{Ri}_B = f^2 b_z^2 b_y^{-4}$. The criteria presented in Thomas et al. (2013) classifies gravitational ($\text{Ri}_B < -1$), mixed gravitational-symmetric ($-1 < \text{Ri}_B < 0$), symmetric ($0 < \text{Ri}_B < 1$ for $\text{Ro}_g < 0$ and $0 < \text{Ri}_B < \text{Ro}_g^{-1}$ for $\text{Ro}_g > 0$), and inertial ($1 < \text{Ri}_B < \text{Ro}_g^{-1}$ for $\text{Ro}_g < 0$) instabilities, as well as stable portions of the water column $\text{Ri}_B > \text{Ro}_g^{-1}$. The geostrophic Rossby number $\text{Ro}_g = \zeta_g f^{-1} \simeq -(\partial u_g / \partial y) f^{-1}$ is computed using the geostrophic alongfront velocity u_g rather than the measured (Thompson et al. 2016). Locations favored for specific submesoscale instabilities as diagnosed by Ri_B are presented in Fig. 9c.

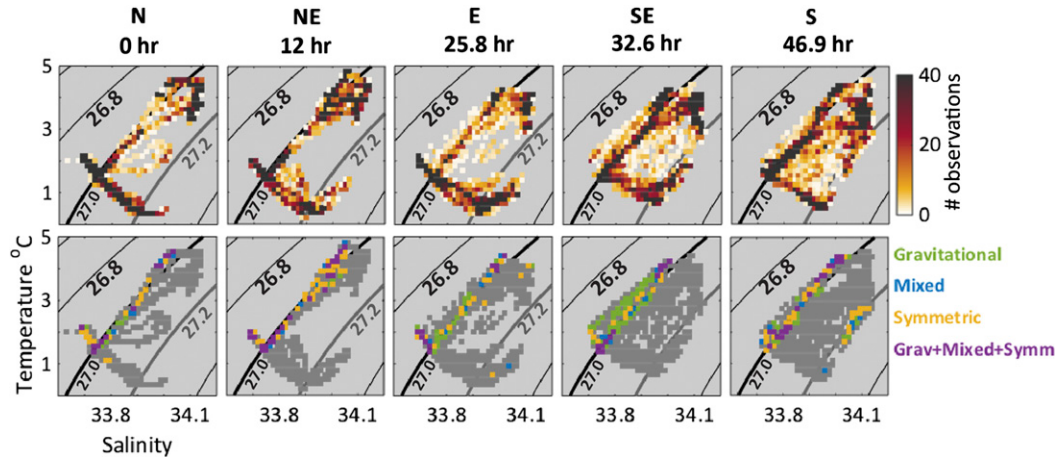


FIG. 10. (a) T - S diagram histograms for Seasoor legs N, NE, E, SE, and S, where color indicates number of measurements in 0.15°C and 0.015 salinity bins and (b) instability types in the mixed layer as diagnosed in section 3d. The cold, fresh observations inside the meander and eddy occupy the bottom-left “hot spot” of measurements in T - S space in leg N. An exchange along isopycnals $\sigma_{\theta27}$ (thick) and $\sigma_{\theta27.2}$ (gray) occurs over this series.

Throughout the survey, the mixed layer was consistently more susceptible to submesoscale instabilities than the deep, stable regions where $\text{EPV} < 0$. Gravitational instability was most likely early in the survey and away from density fronts where MLDs are large. The criteria for mixed and symmetric instabilities are met within density fronts in legs N and E. Conditions conducive for inertial, or centrifugal, instability are located on the outer (right hand) side with $\text{Ro}_g = \zeta_g f^{-1} < 0$.

Regions where conditions are conducive to the development of submesoscale instabilities are shown as a fraction of the mixed layer in Fig. 9d. There is a general decrease between the north and south legs, indicating a greater proportion of the mixed layer is more prone to instabilities earlier in the survey versus in the legs collected in the southern sector of the eddy. Throughout the survey, the majority of the instability indications are for gravitational with conditions favorable for symmetric or mixed gravitational and symmetric concentrated near lateral density gradients.

c. Water mass modification

The sharp temperature and salinity fronts across the eddy boundary (Figs. 7b,c) indicate the presence of different water masses. T - S histograms for Seasoor sections N–S (Fig. 10a) show the prevalence of measurements in 0.15°C and 0.015 salinity bins. In leg N the T - S measurements largely populate two separate regions in T - S space, with cold, fresh inner waters in the bottom left of the diagram and the warm, salty (spicy) outer region measurements in the top right. The two regions in T - S space are connected via $\sigma_{\theta27}$, the isopycnal that outcrops on either side of the dense filament

at the front center in leg N, previously presented in Fig. 7. A similar connection along deeper isopycnals, such as $\sigma_{\theta27.2}$, is not observed in leg N (Fig. 10). This is because of an unequal isopycnal upheaval across the Seasoor leg and the 200-m depth limit of the dataset.

A cross-front exchange is observed in legs NE and E as cool, fresh measurements $\sigma_{\theta27-27.2}$ extend into warmer and saltier T - S space. By leg S, the T - S space is fully populated, indicating mixing or advection of water masses not previously observed at the start of the survey. Locations previously identified as susceptible to submesoscale instabilities in section 4b are shown in T - S space (Fig. 10b). Instabilities are mostly favored along the $\sigma_{\theta27}$, supporting an along-isopycnal exchange across the frontal region. The exchange or modification along $\sigma_{\theta27.1-27.2}$ suggests that water mass properties below the MLD are also affected on time scales of $O(1)$ day and horizontal length scales of $O(1-10)$ km during the formation of this mesoscale eddy.

5. Discussion and summary

Here we have presented high-resolution observations across the ACC as a cyclonic eddy formed in the Scotia Sea. The novel observations reveal submesoscale frontal variability and two distinct dynamic regimes along the periphery of the eddy as depicted in Fig. 11.

In the northern to eastern regime of the survey, diffluent flow and deceleration were observed in the cross-front and alongfront directions, respectively. Along the newly formed southern edge of the eddy, alongfront acceleration and cross-front confluent flow is observed

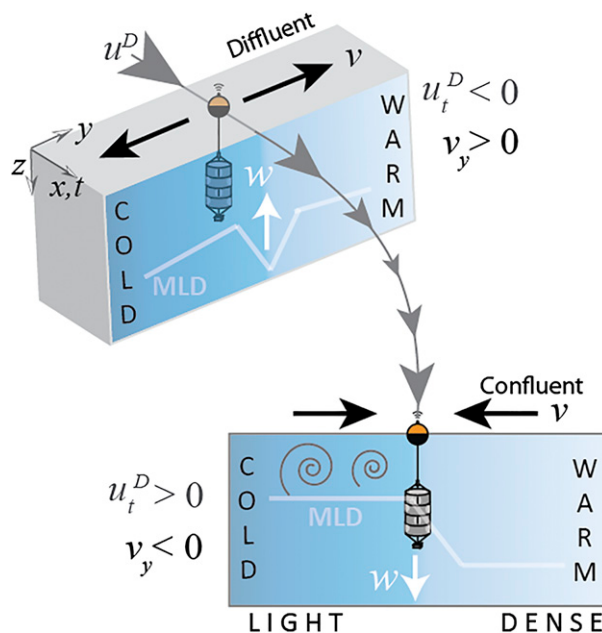


FIG. 11. Cartoon summarizing frontal circulation during eddy formation. The two cross-frontal sections represent the northern and southern sectors of the survey, legs N and S.

coincident with a complex T - S structure, similar to submesoscale features found in other studies, for example, filaments and streamers (Gula et al. 2014; Klymak et al. 2016). A submesoscale instability analysis identified regions across each cross-frontal section prone to the development of gravitational, mixed, symmetric, and inertial instabilities. Favorable conditions for mixed and symmetric instabilities were found near large cross-frontal density gradients in the mixed layer throughout the survey. Despite the loss of frontal integrity observed in the southern regime, the eddy discussed here maintained a distinct signature in SST and SSH over the following two months as evidenced by remote sensing imagery.

The Scotia Sea hosts an especially high abundance of mesoscale eddies (Frenger et al. 2015) in the eddy-rich Southern Ocean. EKE in this region, calculated from time-mean-removed, altimetry-derived geostrophic surface currents (AVISO; 1993–2015) is $O(0.1\text{--}1)\text{ m}^2\text{s}^{-2}$. Recent submesoscale-resolving modeling results indicate a strong correlation between mesoscale EKE and submesoscale vertical velocity in the Southern Ocean (Rosso et al. 2015), implicating a downscale energy transfer. Although the Scotia Sea EKE values and w estimates presented here are much higher than the domain-averaged magnitudes reported in Rosso et al. (2015), the trend of high EKE and high w is consistent.

The strong vertical circulation found at the SAF suggests that submesoscale processes might be critical in transforming and subducting mode and intermediate

waters, although such processes have been mostly ignored in previous studies. Water mass properties across the frontal region were initially observed as a cold, fresh eddy region and a warm, salty outer region. The rapid spread in T - S space suggests mixing occurred during the eddy formation. Enhanced vertical circulation and mixing, prompted by submesoscale processes, have the potential to transform mode and intermediate water density classes and contribute to the uptake of anthropogenic heat and carbon to the Southern Ocean. A quantification of the net water-mass subduction associated with the observed circulation will be part of a future study.

Cyclonic mesoscale eddies have been observed with high chlorophyll signatures in the Scotia Sea (Kahru et al. 2007), implicating their importance on primary production in the region. Studies resolving submesoscale dynamics in mesoscale eddies have shown that strong vertical velocities, like those presented here, may drive the vertical exchange in the upper ocean with important effects on nutrient supply to the photic zone (Lévy et al. 2001; Mahadevan et al. 2008; Lévy et al. 2012; Mahadevan 2016). The biogeochemical responses within the eddy observed during the SMILES cruise are a focus of a future study.

Acknowledgments. The SMILES project is funded through the National Environmental Research Council, standard Grant NE/J009857/1. JR311 data collection and technical support were received from the British Antarctic Survey, the crew of RRS *James Clark Ross*, and the NEODAAS and PML remote sensing groups. Seasoar operations were led by National Marine Facilities technicians Paul Provost, Dougal Mountifield, Julie Wood, and Candice Cameron, from the UK National Oceanographic Centre. Peter Ganderton designed and built the drifter electronics package. The altimeter products were produced by Ssalto/Duacs and distributed by Aviso, with support from Cnes (<http://www.aviso.altimetry.fr/duacs/>). Microwave OI SST data are produced by Remote Sensing Systems and sponsored by National Oceanographic Partnership Program (NOPP) and the NASA Earth Science Physical Oceanography Program.

APPENDIX

Assumptions

The derivation of the vertical velocity presented in section 4a requires two key assumptions. The first relates to the depth range over which the drifter acceleration is valid, and the second requires that the local Eulerian acceleration is much smaller than the drifter acceleration. Both assumptions have critical implications

for the estimate of vertical velocity, and we thus expand on the justification for making these assumptions below.

a. Assumption in (2)

The assumption presented in (2), $(d\mathbf{u}_D/dt) = (d/dt)\{\bar{\mathbf{u}}_E[x_D(t), y_D(t), t]\}$, sets the drifter acceleration equal to the depth-averaged Eulerian acceleration from the drogue depth of 50 m to the surface. If the drifter has a sufficient drag ratio (see section 2), this assumption is justified and $u_D \sim \bar{u}_E$. A comparison of u_D and the \bar{u}_E from 30 to 50 m, presented in Fig. A1a, shows very strong agreement. Because of the blanking distance of the 75-kHz ADCP, measurements of u_E are only available for depths below 30 m. Slab and linear extrapolations from 30 m to the surface are used to approximate \bar{u}_E from 0 to 50 m. The depth-integrated 30–50 m Eulerian velocities and depth-integrated extrapolated 0–50 m Eulerian velocities are compared with the drifter velocities in Figs. A1b and A1c. The slab-extrapolated approximation is a better fit than the linear extrapolation. The calculation of vertical velocity in section 4a is carried out with both extrapolation approximations of u_E (Fig. 8d).

b. Assumption in (11)

The steady state assumption in (11), $(\partial\bar{u}_E/\partial t) \ll (du_D/dt)$, requires the local Eulerian acceleration $\partial\bar{u}_E/\partial t$ in the top 50 m to be much smaller than the drifter acceleration. To check this assumption, we calculate $\partial\bar{u}_E/\partial t$ from ship track intersections during the Seasoor survey, for example, $\partial\bar{u}_E/\partial t \simeq [u_E(t_2) - u_E(t_1)]/(t_2 - t_1)$, where t_1 and t_2 are times corresponding to the ADCP measurements for a given ship track intersection. Measurement pairs are matched if separated by less than 250 m horizontally and more than 1 day in time. The time separation criteria are consistent with the filtering window of the drifter velocities. Nine pairs of measurements were found and used to estimate the local Eulerian acceleration $\partial\bar{u}_E/\partial t$ depth-averaged over 30–50 m. Locations of the measurement pairs are shown in Fig. A2. The average $\partial\bar{u}_E/\partial t$, $-1.3 \pm 1.2 \times 10^{-6} (\text{m s}^{-2})$, is plotted alongside the drifter acceleration time series during the survey. The steady-state assumption [(11)] in section 4a holds for most Seasoor legs where drifter accelerations are larger than the average Eulerian acceleration estimate. In the northeast sector of the eddy and a few southern eddy legs, this is not true and the steady state assumption cannot be made from this ship intersection estimate alone.

Additionally, $\partial\bar{u}_E/\partial t$ is estimated from altimeter-derived geostrophic surface currents (not shown). The average values for the survey region are $0.04 \pm 0.02 \text{ m s}^{-1} \text{ day}^{-1}$, which is an order of magnitude

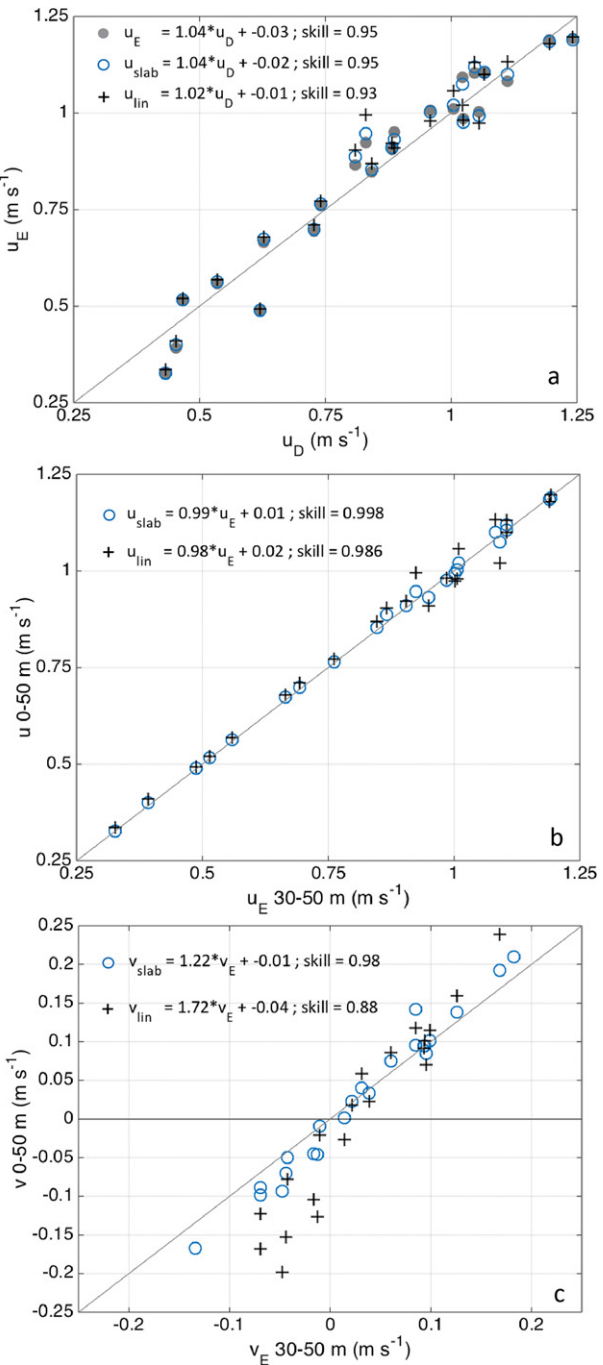


FIG. A1. (a) Drogued drifter velocities (u_D) compared with depth-averaged Eulerian velocities between 30 and 50 m (u_E , ●) and approximations of u_E from 0 to 50 m using slab (○) and linear (+) extrapolations. (b) Comparison of the measured u_E (30–50 m) to the extrapolated approximations (0–50 m). (c) As in (b), but for v_E . Linear regression fits and respective skills, $\text{var}(\text{fit})/\text{var}(\text{data})$, are reported in each panel.

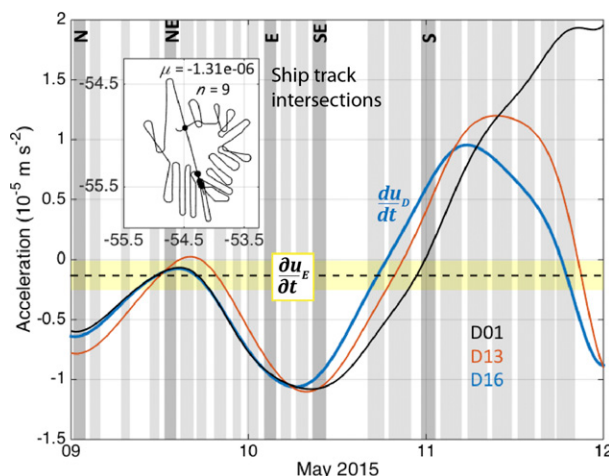


FIG. A2. Estimates of Eulerian local acceleration during the Seasoor survey calculated from ship track intersections (map inset) during the Seasoor survey. Gray bars show the duration of each Seasoor leg; the N, NE, E, SE, and S legs (dark gray) are labeled.

smaller than the average measured drifter accelerations ($0.49 \pm 0.29 \text{ m s}^{-1} \text{ day}^{-1}$) and the opposite sign as an expected change in alongfront velocity due to the cyclonic eddy rotation.

REFERENCES

- Barnes, S. L., 1964: A technique for maximizing details in numerical weather map analysis. *J. Appl. Meteor.*, **3**, 396–409, doi:[10.1175/1520-0450\(1964\)003<0396:ATFMDI>2.0.CO;2](https://doi.org/10.1175/1520-0450(1964)003<0396:ATFMDI>2.0.CO;2).
- Boccaletti, G., R. Ferrari, and B. Fox-Kemper, 2007: Mixed layer instabilities and restratification. *J. Phys. Oceanogr.*, **37**, 2228–2250, doi:[10.1175/JPO3101.1](https://doi.org/10.1175/JPO3101.1).
- Capet, X., J. C. McWilliams, M. J. Molemaker, and A. F. Shchepetkin, 2008: Mesoscale to submesoscale transition in the California current system. Part I: Flow structure, eddy flux, and observational tests. *J. Phys. Oceanogr.*, **38**, 29–43, doi:[10.1175/2007JPO3671.1](https://doi.org/10.1175/2007JPO3671.1).
- Cerovecki, I., L. D. Talley, M. R. Mazloff, and G. Maze, 2013: Subantarctic mode water formation, destruction, and export in the eddy-permitting Southern Ocean state estimate. *J. Phys. Oceanogr.*, **43**, 1485–1511, doi:[10.1175/JPO-D-12-0121.1](https://doi.org/10.1175/JPO-D-12-0121.1).
- Donohue, K., D. Watts, P. Hamilton, R. Leben, and M. Kennelly, 2016: Loop current eddy formation and baroclinic instability. *Dyn. Atmos. Oceans*, **76**, 195–216, doi:[10.1016/j.dynatmoce.2016.01.004](https://doi.org/10.1016/j.dynatmoce.2016.01.004).
- Fox-Kemper, B., R. Ferrari, and R. Hallberg, 2008: Parameterization of mixed layer eddies. Part I: Theory and diagnosis. *J. Phys. Oceanogr.*, **38**, 1145–1165, doi:[10.1175/2007JPO3792.1](https://doi.org/10.1175/2007JPO3792.1).
- Frenger, I., M. Münnich, N. Gruber, and R. Knutti, 2015: Southern Ocean eddy phenomenology. *J. Geophys. Res. Oceans*, **120**, 7413–7449, doi:[10.1002/2015JC011047](https://doi.org/10.1002/2015JC011047).
- Frölicher, T. L., J. L. Sarmiento, D. J. Paynter, J. P. Dunne, J. P. Krasting, and M. Winton, 2015: Dominance of the Southern Ocean in anthropogenic carbon and heat uptake in CMIP5 models. *J. Climate*, **28**, 862–886, doi:[10.1175/JCLI-D-14-00117.1](https://doi.org/10.1175/JCLI-D-14-00117.1).
- Gula, J., M. J. Molemaker, and J. C. McWilliams, 2014: Submesoscale cold filaments in the Gulf Stream. *J. Phys. Oceanogr.*, **44**, 2617–2643, doi:[10.1175/JPO-D-14-0029.1](https://doi.org/10.1175/JPO-D-14-0029.1).
- Haine, T. W. N., and J. Marshall, 1998: Gravitational, symmetric, and baroclinic instability of the ocean mixed layer. *J. Phys. Oceanogr.*, **28**, 634–658, doi:[10.1175/1520-0485\(1998\)028<0634:GSABIO>2.0.CO;2](https://doi.org/10.1175/1520-0485(1998)028<0634:GSABIO>2.0.CO;2).
- Haney, S., B. Fox-Kemper, K. Julien, and A. Webb, 2015: Symmetric and geostrophic instabilities in the wave-forced ocean mixed layer. *J. Phys. Oceanogr.*, **45**, 3033–3056, doi:[10.1175/JPO-D-15-0044.1](https://doi.org/10.1175/JPO-D-15-0044.1).
- Hosegood, P. J., M. C. Gregg, and M. H. Alford, 2008: Restratification of the surface mixed layer with submesoscale lateral density gradients: Diagnosing the importance of the horizontal dimension. *J. Phys. Oceanogr.*, **38**, 2438–2460, doi:[10.1175/2008JPO3843.1](https://doi.org/10.1175/2008JPO3843.1).
- , —, and —, 2013: Wind-driven submesoscale subduction at the north Pacific subtropical front. *J. Geophys. Res. Oceans*, **118**, 5333–5352, doi:[10.1002/jgrc.20385](https://doi.org/10.1002/jgrc.20385).
- Hoskins, B. J., 1974: The role of potential vorticity in symmetric stability and instability. *Quart. J. Roy. Meteor. Soc.*, **100**, 480–482, doi:[10.1002/qj.49710042520](https://doi.org/10.1002/qj.49710042520).
- Kahru, M., B. G. Mitchell, S. T. Gille, C. D. Hewes, and O. Holm-Hansen, 2007: Eddies enhance biological production in the Weddell-Scotia Confluence of the Southern Ocean. *Geophys. Res. Lett.*, **34**, L14603, doi:[10.1029/2007GL030430](https://doi.org/10.1029/2007GL030430).
- Klymak, J. M., and Coauthors, 2016: Submesoscale streamers exchange water on the north wall of the Gulf Stream. *Geophys. Res. Lett.*, **43**, 1226–1233, doi:[10.1002/2015GL067152](https://doi.org/10.1002/2015GL067152).
- Lévy, M., P. Klein, and A.-M. Treguier, 2001: Impact of submesoscale physics on production and subduction of phytoplankton in an oligotrophic regime. *J. Mar. Res.*, **59**, 535–565, doi:[10.1357/002224001762842181](https://doi.org/10.1357/002224001762842181).
- , R. Ferrari, P. J. S. Franks, A. P. Martin, and P. Rivière, 2012: Bringing physics to life at the submesoscale. *Geophys. Res. Lett.*, **39**, L14602, doi:[10.1029/2012GL052756](https://doi.org/10.1029/2012GL052756).
- Mahadevan, A., 2016: The impact of submesoscale physics on primary productivity of plankton. *Annu. Rev. Mar. Sci.*, **8**, 161–184, doi:[10.1146/annurev-marine-010814-015912](https://doi.org/10.1146/annurev-marine-010814-015912).
- , and A. Tandon, 2006: An analysis of mechanisms for submesoscale vertical motion at ocean fronts. *Ocean Modell.*, **14**, 241–256, doi:[10.1016/j.ocemod.2006.05.006](https://doi.org/10.1016/j.ocemod.2006.05.006).
- , L. N. Thomas, and A. Tandon, 2008: Comment on “Eddy/wind interactions stimulate extraordinary mid-ocean plankton blooms.” *Science*, **320**, 448, doi:[10.1126/science.1152111](https://doi.org/10.1126/science.1152111).
- , A. Tandon, and R. Ferrari, 2010: Rapid changes in mixed layer stratification driven by submesoscale instabilities and winds. *J. Geophys. Res.*, **115**, C03017, doi:[10.1029/2008JC005203](https://doi.org/10.1029/2008JC005203).
- Naveira Garabato, A. C., H. Leach, J. T. Allen, R. T. Pollard, and V. H. Strass, 2001: Mesoscale subduction at the Antarctic polar front driven by baroclinic instability. *J. Phys. Oceanogr.*, **31**, 2087–2107, doi:[10.1175/1520-0485\(2001\)031<2087:MSATAP>2.0.CO;2](https://doi.org/10.1175/1520-0485(2001)031<2087:MSATAP>2.0.CO;2).
- Orsi, A. H., T. Whitworth III, and W. D. Nowlin, 1995: On the meridional extent and fronts of the Antarctic Circumpolar Current. *Deep-Sea Res. I*, **42**, 641–673, doi:[10.1016/0967-0637\(95\)00021-W](https://doi.org/10.1016/0967-0637(95)00021-W).
- Pardo, P. C., F. Pérez, S. Khatiwala, and A. Ríos, 2014: Anthropogenic CO₂ estimates in the Southern Ocean: Storage partitioning in the different water masses. *Prog. Oceanogr.*, **120**, 230–242, doi:[10.1016/j.pocean.2013.09.005](https://doi.org/10.1016/j.pocean.2013.09.005).
- Pujol, M.-I., Y. Faugère, G. Taburet, S. Dupuy, C. Pelloquin, M. Ablain, and N. Picot, 2016: DUACS DT2014: The new multi-mission altimeter dataset reprocessed over 20 years. *Ocean Sci.*, **12**, 1067–1090, doi:[10.5194/os-2015-110](https://doi.org/10.5194/os-2015-110).

- Rocha, C. B., T. K. Chereskin, S. T. Gille, and D. Menemenlis, 2016: Mesoscale to submesoscale wavenumber spectra in Drake Passage. *J. Phys. Oceanogr.*, **46**, 601–620, doi:[10.1175/JPO-D-15-0087.1](https://doi.org/10.1175/JPO-D-15-0087.1).
- Rosso, I., A. M. Hogg, A. E. Kiss, and B. Gayen, 2015: Topographic influence on submesoscale dynamics in the Southern Ocean. *Geophys. Res. Lett.*, **42**, 1139–1147, doi:[10.1002/2014GL062720](https://doi.org/10.1002/2014GL062720).
- Sabine, C. L., and Coauthors, 2004: The oceanic sink for anthropogenic CO₂. *Science*, **305**, 367–371, doi:[10.1126/science.1097403](https://doi.org/10.1126/science.1097403).
- Sallée, J. B., K. Speer, and R. Morrow, 2008: Response of the Antarctic Circumpolar Current to atmospheric variability. *J. Climate*, **21**, 3020–3039, doi:[10.1175/2007JCLI1702.1](https://doi.org/10.1175/2007JCLI1702.1).
- , —, S. Rintoul, and S. Wijffels, 2010: Southern Ocean thermocline ventilation. *J. Phys. Oceanogr.*, **40**, 509–529, doi:[10.1175/2009JPO4291.1](https://doi.org/10.1175/2009JPO4291.1).
- , R. J. Matear, S. R. Rintoul, and A. Lenton, 2012: Localized subduction of anthropogenic carbon dioxide in the Southern Hemisphere oceans. *Nat. Geosci.*, **5**, 579–584, doi:[10.1038/ngeo1523](https://doi.org/10.1038/ngeo1523).
- Shakespeare, C. J., 2016: Curved density fronts: Cyclogeostrophic adjustment and frontogenesis. *J. Phys. Oceanogr.*, **46**, 3193–3207, doi:[10.1175/JPO-D-16-0137.1](https://doi.org/10.1175/JPO-D-16-0137.1).
- Sybrandy, A. L., P. P. Niiler, C. Martin, W. Scuba, E. Charpentier, and D. T. Meldrum, 2009: Global Drifter Programme: Barometer drifter design reference. DBCP Rep. 4, Revision 2.2, 47 pp. [Available online at http://www.jcommops.org/doc/DBCP/SVPB_design_manual.pdf.]
- Taylor, J. R., and R. Ferrari, 2009: On the equilibration of a symmetrically unstable front via a secondary shear instability. *J. Fluid Mech.*, **622**, 103, doi:[10.1017/S0022112008005272](https://doi.org/10.1017/S0022112008005272).
- Thomas, L. N., and J. R. Taylor, 2010: Reduction of the usable wind-work on the general circulation by forced symmetric instability. *Geophys. Res. Lett.*, **37**, L18606, doi:[10.1029/2010GL044680](https://doi.org/10.1029/2010GL044680).
- , A. Tandon, and A. Mahadevan, 2008: Submesoscale processes and dynamics. *Ocean Modeling in an Eddying Regime, Geophys. Monogr.*, Vol. 177, Amer. Geophys. Union, 17–38, doi:[10.1029/177GM04](https://doi.org/10.1029/177GM04).
- , J. R. Taylor, R. Ferrari, and T. M. Joyce, 2013: Symmetric instability in the Gulf Stream. *Deep-Sea Res. II*, **91**, 96–110, doi:[10.1016/j.dsret.2013.02.025](https://doi.org/10.1016/j.dsret.2013.02.025).
- , —, E. A. D’Asaro, C. M. Lee, J. M. Klymak, and A. Shcherbina, 2016: Symmetric instability, inertial oscillations, and turbulence at the Gulf Stream front. *J. Phys. Oceanogr.*, **46**, 197–217, doi:[10.1175/JPO-D-15-0008.1](https://doi.org/10.1175/JPO-D-15-0008.1).
- Thompson, A. F., A. Lazar, C. Buckingham, A. C. Naveira Garabato, G. M. Damerell, and K. J. Heywood, 2016: Open-ocean submesoscale motions: A full seasonal cycle of mixed layer instabilities from gliders. *J. Phys. Oceanogr.*, **46**, 1285–1307, doi:[10.1175/JPO-D-15-0170.1](https://doi.org/10.1175/JPO-D-15-0170.1).